

Explosive Disruption of Polytropes: a One Dimensional Hydrodynamic Calculation

Mark C. Wyman^{1,2*}, David F. Chernoff^{1*}, and Ira Wasserman^{1,2*}

¹ Center for Radiophysics and Space Research, Cornell University, Ithaca, NY 14853, USA

² Laboratory for Elementary Particle Physics, Cornell University, Ithaca, NY 14853, USA

Submitted 2004 April 23; Resubmitted 2004 July 19

ABSTRACT

We study explosions of stellar models using a one-dimensional Lagrangian hydrodynamics code. We calculate how much mass is liberated as a function of the energy of explosion for a variety of pre-explosion polytropic structures and for equations of state with a range of radiation-to-gas pressure ratios. The results show that simple assumptions about the amount of mass lost in an explosion can be quite inaccurate, and that even one-dimensional stellar models exhibit a rich phenomenology. The mass loss fraction rises from about 50 to 100 per cent as a function of the explosion energy in an approximately discontinuous manner. Combining our results with those of other, more realistic models, we suggest that Nova Scorpii (J1655-40) may have experienced significant mass fallback because the explosion energy was less than the critical value. We infer that the original progenitor was less than twice the mass of today's remnant.

Key words: supernovae: general, computational; hydrodynamics

1 INTRODUCTION

A fundamental question in the study of supernovae is the fate of a star subject to an explosion of a given strength: is the star completely disrupted, and, if not, how much of the star is lost and what is the configuration of the matter that remains bound? Many researchers have addressed this question for specific cases of interest using detailed numerical simulations. To our knowledge, a precise quantitative relationship between the strength of the explosion and the fate of the outer layers has not been given before, even for highly idealized stellar models. The potential utility of such a relationship is evident in the analysis of Fryer & Kalogera (2001), where a simple “rule of thumb,” introduced to estimate the amount of mass left bound in a supernova, allows a determination of which high mass stars leave behind neutron stars and which ones yield black holes. The “rule of thumb” stipulates that a portion (between 30 and 50 per cent) of the explosion energy is effective in directly unbinding the outermost layers of a star; this estimate is based on detailed simulations by MacFadyen et al. (2001) for a set of specific stellar progenitors.

Our goal is to improve the understanding of the disruption process by carrying out hydrodynamical calculations of simple, polytropic stellar models with a range of explosion strengths, polytropic indices, and equations of state. We in-

tend this sort of calculation to complement, not replace, the realistic, detailed simulations that are the current state-of-the-art in this field. Physical complications such as density jumps, neutrino transport, and aspherical motions are absent from our calculations. Instead, our goal is to incorporate the essential physics – hydrodynamics and gravity – in models that are easy to compute and useful to the study of supernovae in the same way that the polytrope itself is useful to stellar modeling. We note that this subject has been treated before, in a very different perturbative calculation (Nadezhin & Frank-Kamenetskii 1963). Already, our results yield improved versions of the “rule of thumb,” which we provide in a simple, easily applied, empirical form. Although a host of significant core-collapse modeling uncertainties remain (hydrodynamic motions in the core, distribution of angular momentum within the collapsing object, neutrino-matter coupling, etc.), our simplified treatment represents an improvement in the determination of the fate of central remnants – providing a convenient bridge between estimates of mass loss based upon simple physical assumptions and more sophisticated, realistic simulations.

There is considerable evidence that a supernova explosion occurred in J1655-40: the atmosphere of its companion is contaminated with elements thought to be formed only in supernovae (Israelian et al. 1999), and it is likely that the black hole progenitor was considerably more massive than the remnant we see today (Orosz & Bailyn 1997; Shahbaz et al. 1999). There is also some evidence that the J1655-40 system could have remained bound only if it re-

* E-mail: wyman@astro.cornell.edu; chernoff@astro.cornell.edu; ira@astro.cornell.edu

ceived a substantial kick during or shortly after the formation of its black hole (Mirabel et al. 2002). While our current models are too simple to provide definitive results for any particular system, we believe that the methods employed here suggest that the progenitor mass was less than twice the mass of today’s remnant. Mass fallback may trigger the collapse to a black hole as well as pollute the companion’s atmosphere.

In section 2, we describe the physical set up, while section 3 describes the numerical code. In section 4, we give more detailed results and discuss how the numerical data were analyzed, and in section 5 we comment on our results’ lack of dependence on the inner boundary condition.

2 PROBLEM AND PARAMETER RANGES

We model the supernova as a spherically symmetric explosion in a stellar model that is initially in hydrostatic equilibrium. The pre-explosion stellar structure is polytropic. We deposit the full energy of the explosion in a small region near the centre of the polytrope. Using a finite-difference code we calculate the hydrodynamical evolution. A shock propagates towards the surface and the outer layers of the stellar model may be ejected. If it is not completely destroyed, part of the model remains gravitationally bound and we follow the evolution long enough to make an accurate estimate of the mass of the remnant.

We considered a *range of initial stellar structures*. We varied the polytropic index Γ where $P \propto \rho^\Gamma$. The Lane-Emden equation prescribes the run of density and pressure in the initial model; our choices for $n = 1/(\Gamma - 1)$ span $3/2 \leq n \leq 4$. As is well-known, the polytrope’s ratio of central to mean density increases as n varies from 0 to 5. This range subsumes typical main-sequence profiles and extended red-giant structures.

We considered *two equation of state treatments*: ideal gas pressure (“EOS M”: $P = P_{matter}$ with a fixed ratio of specific heats γ) and a mixture of gas plus radiation in thermal equilibrium (“EOS MR”: $P = P_{rad} + P_{matter}$). EOS M is suitable for stellar models of low mass (dominated by particle pressure at their centres) and weak explosions (such that the post-shock gas is not radiation dominated); EOS MR is needed if there is significant radiation pressure. We infer the temperature profile from the appropriate EOS and the Lane-Emden pressure-density profile. For EOS MR, we chose to limit ourselves to *convectively stable polytropic models*. We will discuss the condition for stability in §4.2. To facilitate the description of our problem’s parameter space, let $s_c = P_{rad}(r = 0)/P_{matter}(r = 0)$. As we will show in §4.1, for a given polytropic index n , the choice of s_c uniquely fixes the mass of the resulting stellar model. We define our mass scale to be $M_{scale} = M_\odot(m_p/2\mu)^2$. We then chose the dimensionless masses of the stellar models we exploded to be $\tilde{m} = M_{star}/M_{scale} = 10, 100, 1000$ for a range of (n, s_c) pairs, taking care to remain in the convectively stable region of parameter space. See Tab.1 and Fig.1.

We considered a *variety of explosion energies*. Given our interest in studying explosions which only partially unbind the stellar models, we typically considered blasts with $0.1 \leq E_{blast}/E_{bind} \leq 1.5$, *i.e.* energies of the same order of magnitude as a simple dimensional estimate for unbinding.

In brief, the results we obtained were as follows.

- The amount of mass lost as a function of explosion energy makes a discrete jump from approximately 50 to 100 per cent in all models, suggesting a point of instability.
- Explosions that do not totally disrupt a stellar model give rise to mass loss curves that, in most cases, scale quadratically with explosion energy.

These simulations did not include any sort of compact object at the core of our explosions. We explored the sensitivity of the mass loss to *our treatment of the inner boundary condition*. We found that to a large extent the results are unchanged:

- When two extreme inner boundary conditions – a ‘vacuum cleaner’ core that sucks up any incident material, and its opposite, a hard, reflecting shell – were compared, the mass loss results were virtually identical.

Readers primarily interested in further details regarding these results are encouraged to skip to §4.

3 THE CODE AND NUMERICAL TESTS

3.1 Equations

We use the inviscid fluid equations which describe mass, momentum and energy conservation. All calculations are one-dimensional with either a plane-parallel (for testing) or spherical (for testing and simulations) geometry. We advance the fluid state using a finite difference approximation to the fluid equations (Lax-Wendroff, explicitly differenced, 1-D Lagrangian code [Richtmyer & Morton 1967]). Shocks are handled with the addition of artificial viscosity. We solve Poisson’s equation to determine the gravitational forces at each time step. Details are provided in Appendices A - C.

3.2 Tests of hydrodynamics

We tested the purely hydrodynamic capabilities of the code (no gravity) via comparison with the Sod shock tube (plane-parallel geometry) and Sedov blast (spherical geometry) solutions. For the Sod test with $\gamma = 7/5$ (as well as for a range of other γ ’s), EOS M, various overpressures ($p_2/p_1 = 10, 100, 1000$), and 1200 zones, we found essentially perfect agreement between the numerical and analytic solutions, except for the shock smearing over $\sim 5 - 8$ zones.

For the Sedov problem, we re-derived the solution given in *Fluid Mechanics* by Landau & Lifshitz (1987), thereby finding the correction to that solution’s typographical error (in an exponent) mentioned in Shu’s *Gas Dynamics*. The correction is recorded in Appendix D. We carried out a number of blast wave simulations, varying our choices of EOS and γ . For flows dominated by particle pressure we compared numerical solutions ($\gamma = 5/3$ and $7/5$ for EOS M) with the analytic similarity solution; for flows dominated by radiation pressure we compared several different radiation-dominated numerical solutions ($\gamma = 5/3$, EOS MR) to the $\gamma = 4/3$ similarity solution. The radiation-dominated numerical solutions were generated by explosions yielding high-Mach-number shocks. A range of initial radiation-to-matter pressure ratios s and explosion energies were considered.

One simulation with large constant $s \sim 1000$ and relatively small explosion energy and another simulation with small constant $s \sim 0.1$ and large energy both yielded a radiation-dominated post-shock flows.

In all calculations, the explosion was allowed to expand to well over 100 times the size of the initial “bomb zone.” Comparisons of EOS M runs with analytic solutions were possible throughout the simulation; comparisons of EOS MR runs with the analytic radiation-dominated $\gamma = 4/3$ similarity solution were meaningful only for the part of the simulation in which radiation pressure dominated matter pressure, approximately 4-5 expansion times. With 800 zones, the Sedov test gave close (2–3 per cent) agreement in the relative density, velocity and pressure of the numerical solution and the analytic similarity solution for both particle pressure dominated and radiation pressure dominated flows except in the central-most region.

Two factors contribute to the discrepancies at the centre. First, the innermost zone was treated as an adiabatic expanding/contracting bubble. The entropy of this zone was incorrect but its mass was so small that its impact on the rest of the solution was inconsequential. The explosion results were found to be almost entirely insensitive to alternative methods of treating this innermost zone, provided the treatments were energy conserving. Second, explosive energy was injected in a small, but non-negligible central region (typically the inner 5 per cent of the mass). Quantitative differences between the analytic similarity solution and the numerical solution occurred in the part of the grid used as the “bomb zone” and persisted through the simulation. These differences were not unexpected, as the point-like nature of the explosion in the similarity solution cannot be realized in any finite simulation. We also compared two models for the energy injection at the centre. In one, the “thermal bomb,” an excess of thermal energy equal to the desired explosion energy was added by hand to the core (inner 5 per cent of the mass) of the stellar model, essentially creating an out-of-equilibrium hot core that then expanded rapidly into the stellar envelope. In the other, the “kinetic bomb,” a linear velocity profile carrying the same amount of energy was added to the inner 5 per cent of the mass. Both methods produced identical results outside the “bomb zone.”

3.3 Tests of hydrostatics

With the inclusion of self-gravity forces, we verified that Runge-Kutta integration of the Lane-Emden equations yielded stationary, stable configurations for our time-dependent hydrodynamic evolution equations (finite difference scheme). We checked the long-lived stability for all polytropic indices and radiation-to-gas pressure ratios adopted in this study. Likewise, we tested that the virial theorem was satisfied by the initial configurations.

3.4 Tests of self-gravitating explosions

In the actual runs of the problem of interest, we further verified that the treatment of the central zone made no discernible difference, that variations in the size of the “bomb zone” (3-10 per cent, for instance), caused only very slight

(< 5 per cent) changes to the amount of mass lost in the explosions. We also verified that energy conservation was satisfied (to < 5 per cent).

4 RESULTS

We adopted polytropes for the initial stellar structure with $P = k\rho^\Gamma$. The density and pressure profiles were determined by solving the Lane-Emden equation with the total mass and radius scaled to unity. We refer to this as the dimensionless solution; it depends only upon Γ . The dimensionless density-pressure distributions are the forms used in our computations. All results are likewise reported using dimensionless quantities (explosion energy in terms of binding energy, mass loss in terms of the total mass, etc.).

4.1 Scaling of polytropes

Let us first review the scaling of the initial polytropic solution. For given k and $\Gamma \equiv 1 + 1/n$ in the pressure-density relation, it is possible to generate a one-parameter family of scaled solutions with

$$M^{2-\Gamma} R^{3\Gamma-4} = (k/G)f(\Gamma), \quad (1)$$

with $f(\Gamma)$ a dimensionless number depending on polytropic index. We can construct a polytropic progenitor without radiation pressure, but that is an idealization that is approximately correct only in the limit of a low ratio of radiation to gas pressure. If the matter has an ideal gas equation of state, $P = \rho kT/\mu$, there must be nonzero temperature inside the stellar model, and hence nonzero radiation pressure $P_{\text{rad}} = aT^4$. Under some circumstances, P_{rad} will be low both in the progenitor and in the ejecta after the stellar model explodes. The explosions of such models have a universal mass loss fraction as a function of Γ and explosion energy in units of the stellar binding energy.

Imposing a fixed value of the radiation-to-gas pressure $s(r=0) = s_c$ at the centre of the stellar model before the explosion reduces the scaling of the dimensionless solution. These models also have a universal mass loss fraction as a function of Γ , s_c , and explosion energy. The reason the scaling is reduced is because specifying s_c determines the stellar mass for a given value of Γ independent of k :

$$M = m(\Gamma)M_{\text{Ch}}s_c^{1/2}(1+s_c)^{3/2}, \quad (2)$$

where $M_{\text{Ch}} = (\hbar c/G)^{3/2}\mu^{-2} = 1.86(m_p/\mu)^2 M_\odot = 7.44M_{\text{scale}}$, and $m(\Gamma) = (45/\pi^2)^{1/2}[f_\rho(\Gamma)]^2[f_p(\Gamma)]^{-3/2}$, with $f_p(\Gamma) = P_c R^4/GM^2$ and $f_\rho(\Gamma) = \rho_c R^3/M$, which are both dimensionless functions of polytropic index only. For $n = 3/2$, $f_\rho = 1.430$ and $f_p = 0.7702$, so $m(5/3) = 6.460$; for $n = 3$, $f_\rho = 12.94$, $f_p = 11.05$, so $m(4/3) = 9.734$. In the low mass limit, this implies $s_c \propto M^2$. Thus, from Eq. (1), the combination $kR^{4-3\Gamma}$ is determined given Γ and s_c . Recovering the $s_c \rightarrow 0$ limit is subtle, since it also implies low mass M . To summarize: for EOS MR, we use Eq. (2) to solve for s_c given M in terms of $M_{\text{scale}} \equiv (m_p/2\mu)^2 M_\odot$.

In this paper we will adopt the point of view that k is not known *a priori* and we will allow scaling of the polytropic solution to arbitrary M and R in cases with no radiation pressure. In cases with radiation pressure, although M is determined from Eq. (2), some scaling remains since Eq. (1)

relates R and k , given M and Γ , but does not determine either one separately.

4.2 Convective Stability of Polytropes

If we begin with the First Law of Thermodynamics,

$$TdS = dE + PdV, \quad (3)$$

and use EOS MR, together with some of the relations derived in Appendix B, we can put it in the form

$$TdS = f(s, n)dP/\rho. \quad (4)$$

Since $dP/dr < 0$, local convective stability requires $dS/dP < 0$. The condition is

$$n > n_{crit} = \frac{3(8s_r + 1)(s_r + 1)}{8s_r^2 + 13s_r + 2}, \quad (5)$$

where we have used $s_r = s(r) = P_{rad}(r)/P_{matter}(r)$ to distinguish between this function of r and the constant parameter s_c . For stability, we require that the local condition be satisfied throughout the model. The variation of s_r depends upon n :

$$s_r(1 + s_r)^4 \propto \frac{P^3}{\rho^4} \propto P^{\frac{3-n}{1+n}}. \quad (6)$$

There are three characteristic cases

(i) For $n < 3$, the largest value of s_r is $s_c = s(r = 0)$, so the largest value of n_{crit} is $n_{crit}(s_c)$ and therefore if $n > n_{crit}(s_c)$, the stellar model is stable.

- For all $0 \leq s_r \leq \infty$, Eq. (5) implies $n_{crit}(s_r) \geq 3/2$, so no polytrope with $n < 3/2$ can be stable.

- For $3/2 < n < 3$, there is a maximum value of s_c for which the stellar model is stable, determined from $n = n_{crit}(s_c)$, which rises from $s_c = 0$ at $n = 3/2$ to $s_c \rightarrow \infty$ for $n = 3$. For instance, at $n = 2.0$, $s_c^{MAX} = 0.3$; for $n = 2.5$, $s_c^{MAX} = 1.674$ (see Tab. 1 and Fig. 1).

(ii) For $n = 3$, s_r is constant. Since $n_{crit}(s_r) < 3$ for any finite s_r , all models are stable.

(iii) For $n > 3$, $s_r \rightarrow \infty$ at the polytrope's edge (where $P \rightarrow 0$), so for any choice of s_c the largest value of $n_{crit}(s_r) \equiv 3$. All models are stable.

It is important to emphasize that the convective-stability condition described here is not an absolute stability criterion. Stellar models outside of this mass range can certainly exist; they will simply have convection zones. The unstable region in Fig. 1 arises because of our insistence on an exact polytropic pressure-density relation ($P = \kappa\rho^\Gamma$) and our use of EOS MR. We restrict our studies to stable models. These already span a wide range of density profiles – which is the basic physical property that governs shock propagation – from the highly centrally-condensed $n = 4$ polytropes to the diffuse $n = 2$ models. An unstable (polytropic) model would represent an unphysical and unnatural initial state. Actual convective stars involve physics beyond the scope of our simple, idealized, one-dimensional approach.

4.3 Description of Analysis

The chief way in which we shall summarize the results of an explosion is in terms of the mass ejected as a function of explosion energy. We begin by discussing how we extracted the

Table 1. Summary of the parameters describing the models we have studied, where $\tilde{m} = M_{star}/M_{scale}$.

n	\tilde{m}	s_c
2.0	10	0.0256
2.5	“	0.0227
3.0	“	0.0181
4.0	“	0.0117
2.5	100	0.5965
3.0	“	0.5515
4.0	“	0.4219
3.0	1000	2.995
4.0	“	2.600

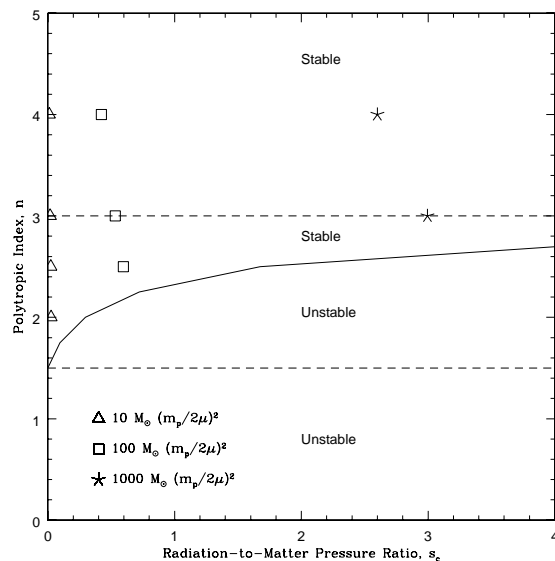


Figure 1. A plot summarizing the results of the stability analysis described in §4.2. Convectively stable and unstable regions of the $n - s_c$ parameter space are labeled, and the models we have selected from this parameter space are marked.

ejected mass from the numerical simulations. For EOS M (no radiation pressure), the code was run until the remnant core had become stationary and had nearly reassumed hydrostatic equilibrium, *i.e.*, it had local gas velocities near zero ($< 10^{-7} R_{stellar}/\text{dynamical time}$) and satisfied the virial theorem. The mass loss was determined by finding the location in the Lagrangian grid of the outermost outgoing zone for which the local energy per unit mass (sum of kinetic, thermal and gravitational contributions) changed from negative to positive (see arrow in Fig. 2). A graph of the local energy density for a typical stellar model after an explosion is included as Fig. 2.

A drawback of this method is apparent in Fig. 2. Though there are distinct portions of the stellar model that can definitely be said to be either remnant or ejecta, there is also a small region with nearly zero energy, resembling an atmosphere around the remnant. These atmospheres did not appear in all explosions – typically, they occurred when $E_{blast} \sim 0.7 - 1.0 E_{bind}$. In some cases, it was adequate sim-

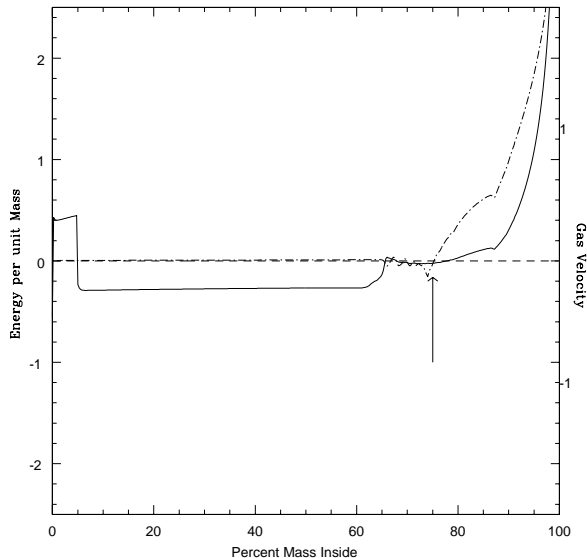


Figure 2. The asymptotic dimensionless local energy per unit mass ($U/(GM_{star}/R_{star})$) (solid line) for $n = 3$ polytrope (no radiation pressure) and $E_{blast} = E_{bind}$ after the central core has reattained hydrostatic equilibrium. The dash-dotted line gives the dimensionless local velocity ($v/(GM_{star}/R_{star})^{1/2}$). The dashed line is a reference line for zero energy and velocity.

ply to run these models longer, with a clear bifurcation point eventually emerging.

When we began to use EOS MR, however, our results remained ambiguous even after long integration times. Thus, we moved to a more detailed procedure for deciding which mass shells were ejecta and which composed the remnant (see Fig. 3). We stored the location and local energy density of each grid zone throughout the run. We then plotted the location of each mass element as a function of time, using the sign of the local energy density to color code the lines. During the atmospheric motions some layers do work on other layers; the color coding shows changes from bound to unbound (and vice-versa). These plots proved to be helpful, illuminating the transient identities of bound atmospheres, marginally bound gas, and low energy ejecta. We adopted the following criterion for ending the calculation: when all outer shells had positive energy density and the number of intermediate shells with local energy density still changing sign was small – less than a couple of percent of the total mass. An example is shown in Fig. 3, where the apparent bifurcation point between bound and unbound material is marked on the far right. Note the diminishing amount of mass ejected with each stellar oscillation. We are confident of this prediction because it was borne out in all cases where the code was run much longer, and, hence, closer to the point of the remnant’s return to hydrodynamic stability.

These plots illustrate two distinct ways in which shells are ejected in successful explosions that are not yet large enough to destroy completely the stellar model: 1) Some shells are lost in the initial shock wave; these gain tremendous kinetic energies. The amount of mass lost in this way is typically ≤ 12 per cent. 2) The rest of the ejecta are expelled by the ringing down of the remnant.

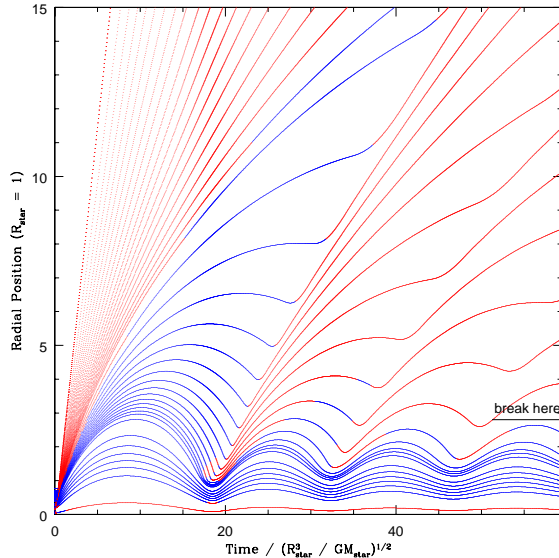


Figure 3. A typical graph of the motion of grid zones in time for an exploding stellar model, in this case an $\tilde{m} = 100$ polytrope of index $n = 3$ with an explosion energy of 90 per cent of the stellar model’s binding energy. Each line tracks a representative mass shell. The Lagrangian mass intervals vary: lines in the ejected region and outer parts of the remnant – which represent escaping mass (large radii) and the uppermost parts of the cooling, bouncing remnant (the blue lines) – are at intervals of 0.5 – 1 per cent of the total mass. In the inner part of the remnant, each line represents approximately 10 per cent of the total mass. Where lines are red, the local energy density is positive; where blue, negative. The bifurcation point separating the remnant from the ejecta is marked. Radial distances are given in units of the initial stellar radius; times are given in dimensionless units defined by $t/(R_{star}^3/GM_{star})^{1/2}$.

We next investigated the extreme limits: total disruption explosions and failed explosions (no ejected mass). Total disruptions were relatively easy to recognize: all grid zones acquired positive energy in the first pass of the shock wave from the explosion. For explosion energies near the threshold for total stellar disruption, however, we found that there was typically a range of energies where a large portion of the stellar envelope was ejected, while leaving an extended remnant undergoing very slow, long-scale oscillations. The precise mass loss in most of these cases was impossible to determine, though it was always ~ 50 per cent. Artificial viscosity eventually damps these oscillations, but it takes a long time to do so. Total disruption happens abruptly, with every stellar model studied going from the ~ 50 per cent mass loss oscillatory state to 100 per cent mass loss with only a small increase in explosion energy. We were able to pin down the width of the transition from remnant to total disruption as function of explosion energy to $\sim 5 - 10$ per cent in the stellar model’s binding energy.

The failed explosion regime was computationally easier to study. Failed explosions produced no unbound shells. The results can be understood in terms of the varying shock speed. Strong shocks slowed as they plowed through the dense core of the stellar model, then accelerated when they reached the steep density gradient of the outer regions of

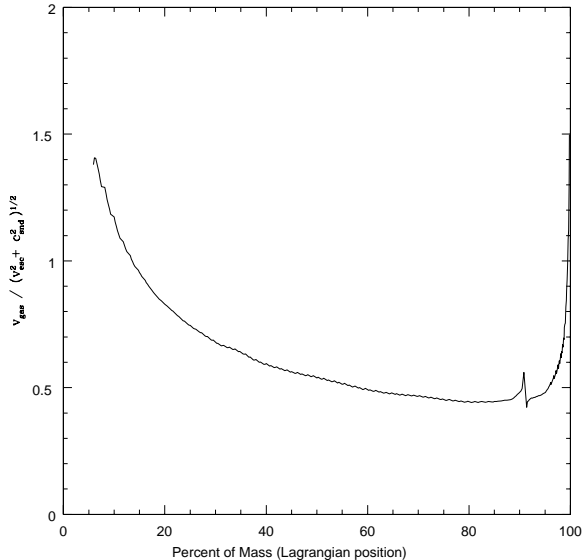


Figure 4. A plot of the $v_{gas}/\sqrt{v_{esc}^2 + c_{snd}^2}$, in this case for a stellar model with $n = 1.5$, $\tilde{m} = 0.55$, and an explosion energy equal to 15 per cent of the stellar model’s binding energy. The choppiness in the plot is due to non-physical effects in the determination of the exact location of the shock. Note the deceleration through the bulk of the stellar model, with only the very outermost shells reaching escape velocity as the shock accelerates in the falling density profile near the edge.

the polytropes. In failed explosions the shock velocity fell below the sound speed in the middle region and/or failed to accelerate up to the local escape speed in the outer region. A plot of the process is included in Fig.4. In the figure, we plot $v_{shock}/\sqrt{v_{esc}^2 + c_{snd}^2}$ – where v_{esc} is the escape velocity for the initial stellar model and c_{snd} is the local sound speed – illustrating the falling shock Mach number in the core and the reacceleration to velocities allowing escape by the large, negative, outward-going density gradient. The physics of this variable shock velocity, including spherical curvature effects and photon loss, are discussed in detail in Matzner & McKee (1999).

4.4 Explosions without radiation pressure

For the first round of explosions, we used EOS M (no radiation pressure). For these calculations, the solution’s independent parameters are E_{blast}/E_{bind} and the stellar model’s polytropic index n .

We have included two figures summarizing the mass loss results. In the first, Fig. 5, the explosions are compared with each other, showing great similarity among the models. In Fig. 6, we have separated each polytrope into its own window to compare its mass loss curve to a couple of “rules of thumb” (Fryer & Kalogera 2001). The first line, the dash-dotted curve, is the simplest such rule. It represents the mass loss if 100 per cent of the explosion energy were distributed in such a way as to eject as many of the outer shells as possible, while leaving untouched those parts of the stellar model which remain bound. This is, of course, physically impossible, but it does provide an upper bound on mass

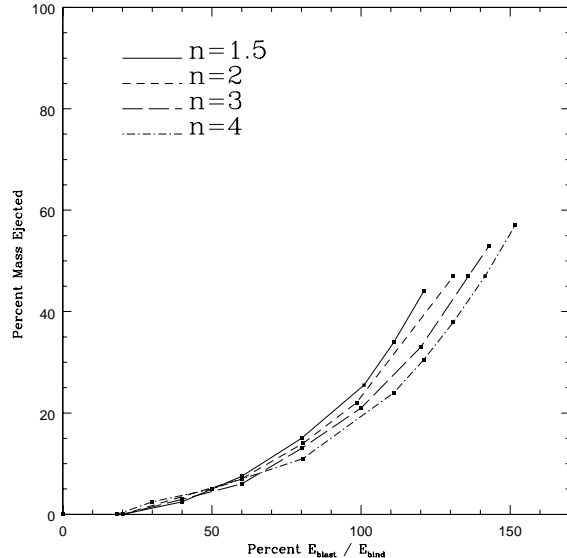


Figure 5. This figure summarizes the mass loss percentages resulting from explosions in polytropes of four different indices without radiation.

loss. The dashed curve represents the actual choice made by Fryer & Kalogera (2001), which essentially splits the explosion energy budget in two, giving 50 per cent to unbinding the stellar model directly, and 50 per cent to heating the remnant and to accelerating the ejecta. This version gives results that are much closer to our numerical calculation, but *overestimates mass loss in low energy explosions* and also *overestimates the amount of energy required to unbind the stellar model completely*.

4.5 Explosions with radiation pressure

For the second round of explosions, we used the hydrodynamics code with EOS MR (matter and radiation pressure). The parameter space now included three variables: explosion energy, polytropic index, and M_{star} . We chose three stellar masses, $\tilde{m} = 10, 100, \text{ and } 1000$, and then surveyed the range of polytropic indices for convectively stable models. For each stellar model, we varied explosion energy from cases of failed explosions to total stellar disruption. The results of these explosions are summarized in Figs. 7, 8, and 9. Because of the difficulty of precisely determining the line of bifurcation between remnant and ejecta even in plots like Fig. 3, error bars have been included. They represent the range within the stellar model where the bifurcation point may occur. This range of uncertainty was determined by finding the region of the stellar model containing either outgoing zones with negative local energy density, located at several stellar radii, or infalling zones with positive local energy density. We considered these to have ambiguous fates. The number of these zones is always small, comprising at the most a couple of percent of the stellar mass. Bold dots are placed at the midpoint of this range.

The mass-loss curves are remarkably uniform, especially given the wide variation in binding energy among the stellar models that we studied (more details on binding energy are

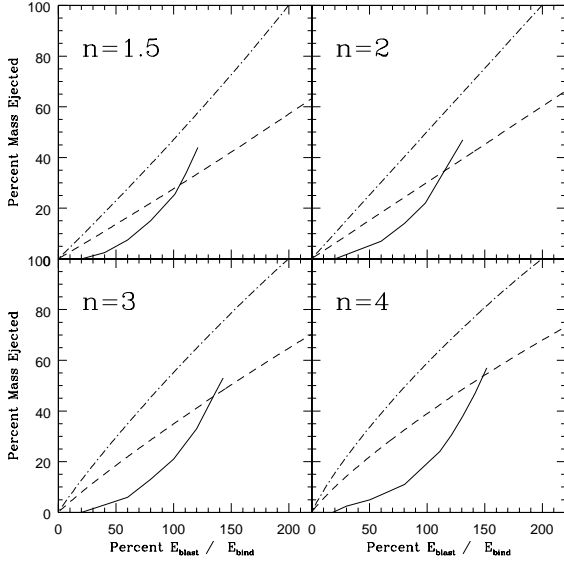


Figure 6. Mass loss curves are compared with two simple assumptions relating explosion energy and mass loss. The dashed curve represents the most efficient possible application of the explosion energy to mass loss. The dash-dotted curve represents the more physically reasonable assumption that 50 per cent of the energy goes into unbinding part of the stellar model, and 50 per cent goes into both heating the remnant and to net kinetic energy for the ejecta.

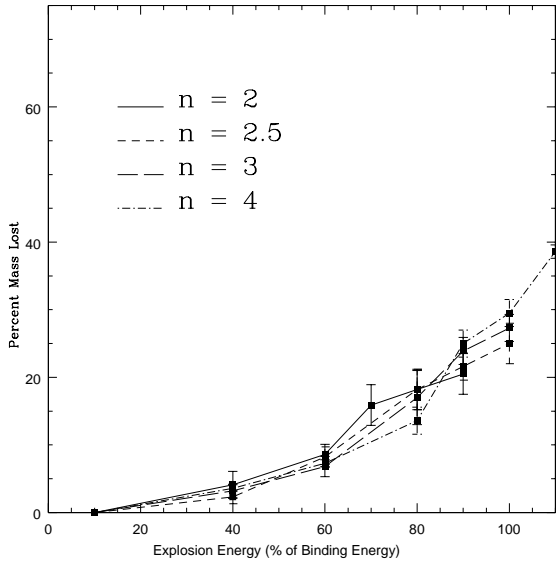


Figure 7. This figure summarizes the mass loss percentages for explosions in $\tilde{m} = 10$ stellar models. Error bars represent the uncertainty in the determination of the remnant - ejecta bifurcation point.

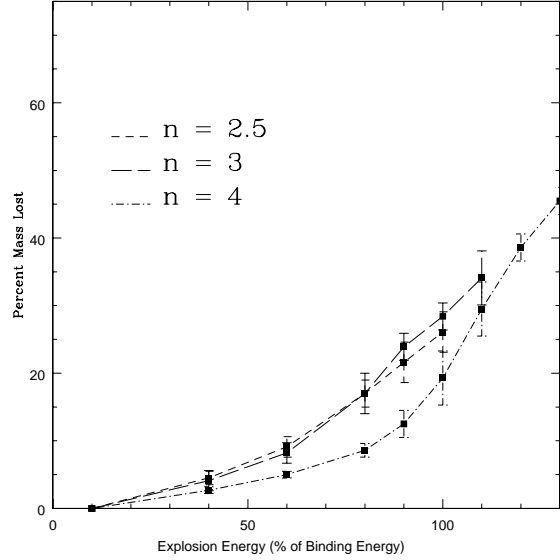


Figure 8. This figure summarizes the mass loss percentages for explosions in $\tilde{m} = 100$ stellar models. Error bars represent the uncertainty in the determination of the remnant - ejecta bifurcation point.

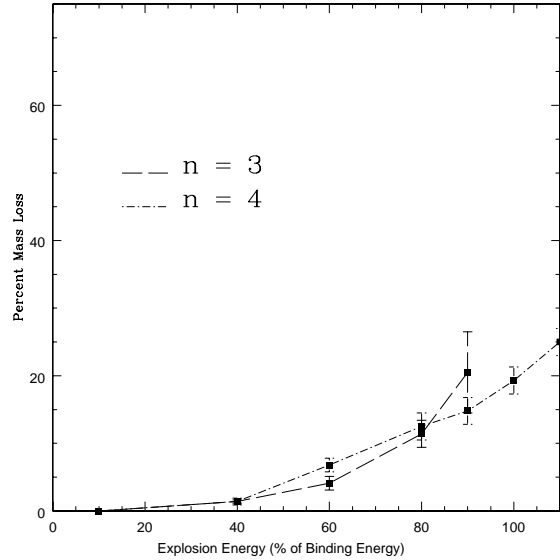


Figure 9. This figure summarizes the mass loss percentages for explosions in $\tilde{m} = 1000$ stellar models. Error bars represent the uncertainty in the determination of the remnant - ejecta bifurcation point.

given in Appendix B). The uniformity in the shapes of the mass-loss curves found allows them to be described accurately by a fitting formula. The form that best fits the data is

$$100 \times \frac{M_{\text{lost}}}{M_{\text{star}}} = \begin{cases} 0 & e < e_o \\ A(e_{\text{blast}} - e_o)^2 & e_o < e < e_f \\ 100 & e_f < e \end{cases} \quad (7)$$

where e_{blast} (e_o , e_f) is blast energy (minimum blast energy

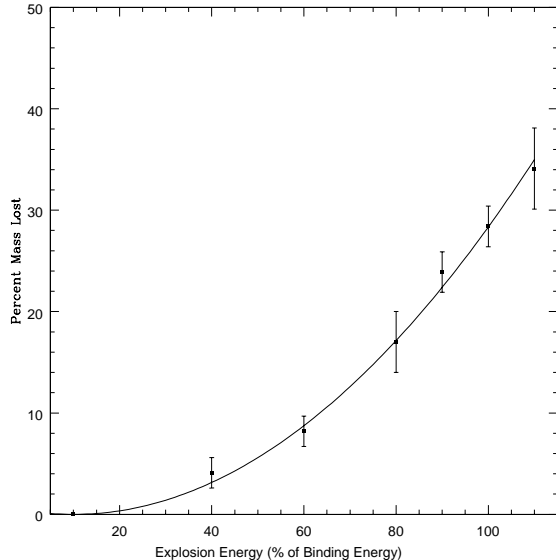


Figure 10. A figure comparing the results of the fitting formula, Eqn. 7, to the data, in this case for an $n = 3$, $\tilde{m} = 100$ stellar model.

Table 2. Summary of fitting parameters for various explosion scenarios. $e_o = 100 \times E_o/E_{\text{bind}}$, $e_f = 100 \times E_f/E_{\text{bind}}$

n	\tilde{m}	$A(\times 10^{-3})$	e_o	e_f
2.0	10	3.57	10	110
2.5	“	3.37	11	120
3.0	“	3.47	10	120
4.0	“	3.67	10	130
2.5	100	2.89	5	120
3.0	“	3.50	10	130
4.0	“	2.95	11	140
3.0	1000	3.74	20	110
4.0	“	2.44	10	130

to cause mass loss, maximum blast energy to leave a bound core) measured as a percent of binding energy (*i.e.* $e_{\text{blast}} = 100 \times E_{\text{blast}}/E_{\text{bind}}$, etc.) and A is the fitting parameter. A sample comparison between the fits and the numerical data is shown graphically in Fig. 10; the parameters describing each model’s fit are contained in Table 2.

Notice that in all cases, total disruption occurs near or slightly above the original stellar binding energy, *i.e.* at $E_{\text{blast}} = (e_f/100)E_{\text{bind}} \gtrsim E_{\text{bind}}$. The transition to total disruption is also very abrupt. Just below e_f , the amount of mass lost is below 50 per cent in all cases.

5 SENSITIVITY TO INNER BOUNDARY CONDITIONS

Our previous results show that mass loss occurs in two distinct phases when the stellar model is not completely unbound. The initial shock wave drives off some mass immediately while the ringing down of the remnant expels loosely bound outer shells over a period of several dynamical times.

None of our models included a compact object at the centre and one naturally wonders whether the later mass loss might be sensitive to the treatment of the centre of the stellar model.

To test the effect of the inner regions on the mass loss, we considered two different ways of modifying the inner boundary condition. In one, we placed a hard, reflecting sphere at a fixed, very small spatial radius; in the other, we fixed a perfectly absorbing boundary at a given radius. We ran several cases: polytropes of indices n between 1.5 and 4, with a variety of values of \tilde{m} . For the reflecting sphere, the size was set to that of the innermost zone; for the absorbing sphere, the absorbing boundary varied between 2 and 30 per cent of the mass in Lagrangian coordinates.

The mass loss computed with these altered inner boundary conditions differed little from what was found in our earlier survey. The changes to the mass loss were unnoticeable even when quite a large inner region – as much as 15 - 20 per cent, in mass – of the stellar model was allowed to become pressure-free and perfectly absorbing. This insensitivity is linked to the fact that at least 50 per cent of the star remains bound if the star survives the explosion. In those cases, on the one hand, the trading of energy among the outer shells determines the amount of mass lost; the inner half of the stellar model, whose dynamics are sensitive to the treatment of the inner zones, is never in danger of being lost. In stellar models that are totally dispersed, on the other hand, the explosion is so violent that differences in the inner boundary conditions have little effect, since no portion of the stellar model ever falls back to experience them.

To gain a better qualitative understanding of why the mass loss results are so insensitive to the inner boundary condition, we examined more closely the slowly-varying disturbances propagating in our remnant. The energy density in a small-wavelength oscillatory mode is proportional to local density times the square of local gas displacement (*e.g.* Christensen-Dalsgaard 2003). We computed this combination – as well as local velocity squared times local density – as a function of radius at various times in our models, using each Lagrangian zone’s displacement from its final, at-rest location. We found that both quantities always go to zero at the remnant core, implying that there is little energy flux into or out of this region. Therefore, information about the altered inner boundary conditions is not effectively transmitted to the oscillating outer mass shells. The inner boundary condition plays no obvious role in the late-time mass loss so long as there is a sufficient amount of buffering gas between the inner core and the outside of the star. In our numerical tests, we found that it was necessary to alter almost the entire inner quarter of the stellar model’s mass before the mass loss was significantly affected.

6 CONCLUSION

Here, we have confined ourselves to a rather idealized problem, partially disruptive explosions of simplified stellar models whose density profiles are solutions to the Lane-Emden equation, but with varying ratios of radiation to matter pressure. In this way, we have been able to survey models in a well-defined parameter space fairly extensively, trading the concreteness of real stellar models for the flexibility of

parametrized ideal models. Specifically, we have determined the fraction of the original stellar mass ejected as a function of explosion energy in polytropes of index $n = 1.5, 2, 3,$ and 4 in calculations without radiation pressure; we also explored the mass loss fractions for stellar models of $\tilde{m} = 10, 100,$ and 1000 over a range of n from 2.0 to 4.0 . Our results suggest that the mass loss is remarkably uniform, even among widely varying stellar density profiles and over an enormous range in stellar masses. We have provided a simple, parametrized formula for the fractional mass loss as a function of explosion energy for a range of values of n and the ratio of radiation to matter pressures; see Eq. (7) and Table 2.

One striking feature of all the models we tested was that the mass loss fraction as a function of explosion energy appears to be discontinuous at around 50 per cent mass loss, with a small (few per cent) difference in explosion energy separating stellar models which lose half their mass from totally disrupted stellar models. Because our simulations did not include formation of a compact remnant at the centre, this result cannot be taken as a concrete demonstration that the observation of a black hole of mass M demands a progenitor whose mass was less than about twice as large.

The abrupt transition between moderate (*i.e.* $\lesssim 50$ per cent) and total disruption found here for wide classes of initial models is also seen in modelling of explosions in sets of specific progenitors (*e.g.* Woosley & Weaver 1995, Table 3; MacFadyen et al. 2001, Table 1). Thus, we conjecture that even when a compact central remnant is included, the results divide into two separate cases depending on whether the explosion energy is above or below, approximately, the critical value found here for complete disruption. It is significant that this bifurcation effect occurs, as it does in our simulation, at the most basic, hydrodynamic level, implying that its appearance in more sophisticated models rests chiefly on these underlying physics. For explosion energies below this critical value, there is a sharp transition between modest (*i.e.* $\lesssim 50$ per cent) mass loss and total disruption apart from the compact remnant. For explosion energies above the cutoff, either a black hole or neutron star may form. However, in this case, we expect much smaller fallback masses, generally only a few tenths of M_{\odot} or less, primarily caused by reverse shock propagation through the core, and the consequent deceleration of a small amount of outgoing matter (*e.g.* Woosley 1988; Chevalier 1989).

We should emphasize that our conjectures here may be significantly modified by the inclusion of more realistic physics. Spherically-symmetric polytropic stellar models are not real stars; neither are all the complexities of stellar hydrodynamics captured by simple equations of state. One important component of realistic stars that our models lack is the sequence of density discontinuities that emerge in evolved stars, which we would expect to cause reflected reverse shocks that could change the mass ejection dynamics considerably. Furthermore, in real supernovae there are other sources of energy besides the initial explosion – such as decaying radioactive nuclei, central pulsars or jets – which continue to add energy to the supernova system at late times, possibly giving the boost needed to eject lightly-bound gas at the surface of the remnant. Our imposition of spherical symmetry is also unrealistic: real explosion are likely to be anisotropic, and stellar rotation, convection,

and magnetic fields are expected to have effects that a one-dimensional calculation cannot hope to model. Despite these caveats, we believe our chief results to be robust.

Supernovae frequently occur in binary systems. In such systems, when there are very energetic explosions and little mass fallback, we expect little mass contamination of the atmosphere of the binary companion. The outgoing regions of the progenitor intercepted by the companion are not captured; indeed the outer layers of the companion are stripped and ablated by the ejecta. On the other hand, when the explosion is weak and substantial mass fallback occurs, progenitor material may fall back onto the companion, polluting its atmosphere. In the latter cases, we would then infer that a remnant of mass M was most likely derived from a progenitor with mass less than $\simeq 2M$. Thus, in systems like Nova Scorpii that show evidence for black hole formation in a supernova (*e.g.* Israelian et al. 1999), we conjecture that mass of the pre-explosion star was, in fact, less than twice the present mass inferred for the black hole remnant (which also has accreted matter since forming, presumably). This may have implications for the dynamics of such systems (*e.g.* Mirabel et al. 2002). We caution, though, that our results may be altered somewhat in more refined models. Further studies are underway to include a compact central remnant, density jumps (expected as a consequence of compositional inhomogeneity), rotation and explosion asymmetries. These new calculations will continue, in the same spirit as those reported here, to employ the simplest explosion models needed to reveal the underlying physical consequences of the various refinements, and to allow a survey of the hydrodynamics of a large range of explosion models.

ACKNOWLEDGMENTS

This research was supported in part by NASA-ATP grant NAG5-8356. M.W. is supported by an NSF Graduate Fellowship. I.W. acknowledges the hospitality of KITP, which is supported by NSF grant PHY99-07949, where part of this research was carried out, as well as support from NSF Grant AST-0307273 and from IGPP at LANL.

REFERENCES

- Chevalier, R. A. 1989, ApJ, 346, 847.
- Christensen-Dalsgaard, J. 2003, Lecture Notes on Stellar Oscillations, <http://astro.phys.au.dk/~jcd/oscilnotes/>, Ch. 5.
- Fryer, C. L. & Kalogera, V. 2001, ApJ, 554,548.
- Israelian, G., Rebolo, R., & Basri, G., 1999, Nat, 401, 142.
- Landau, L. D., and Lifshitz, E. M. 1987, Fluid Mechanics, Pergamon Press: Oxford.
- MacFadyen, A. I., Woosley, S. E., & Heger, A., 1999, ApJ, 524, 262.
- MacFadyen, A. I., Woosley, S. E., & Heger, A., 2001, ApJ, 550, 410.
- Matzner, Christopher D. & McKee, Christopher F. 1999, ApJ, 510,379.
- Mirabel, I. F., Mignani, R., Rodrigues, I., Combi, J. A., Rodríguez, & L. F., Guglielmetti, F. 2002, A&A, 395, 595.

- Nadezhin, D. K. & Frank-Kamenetskii, D. A. 1963, *Soviet Astronomy*, 6, 779.
- Orosz, J. & Bailyn, C. 1997, *ApJ*, 477, 876
- Richtmyer, R. & Morton, K. W. 1967, *Difference Methods For Initial-Value Problems*, John Wiley & Sons: New York
- Shahbaz, T, van der Hooft, F, Casares, J, Charles, P. A., & van Paradijs, J. 1999, *MNRAS*, 306, 89
- Shu, Frank. 1992, *The Physics of Astrophysics: Gas Dynamics*, Volume II, University Science Books: New York.
- Woodsley, S. E. 1988, *ApJ*, 330, 281.
- Woodsley, S. E. & Weaver. T. A. 1995, *ApJS*, 101, 181.

APPENDIX A: DIFFERENCE EQUATIONS

The Lax-Wendroff difference equations for the equations of hydrodynamics in one dimension with spherical symmetry are as follows. Note that the pressure in the equation for advancing energy must be solved for using the equation of state to make this set of difference equations explicit rather than implicit. In the difference equations, n represents time steps, while j represents spatial steps. The equations are non-dimensionalized simply, with each variable scaled to order unity for the initial conditions in all calculations we have done. The one remaining constant, ρ_o , with units of density, sets the overall scale of the system studied. The variable R records the position of each shell. Comparing each shell's current position, R , with r , a static, reference grid, allows the gas's local density to be calculated. The remaining variables are interdependent. The equation for moving grid zones is:

$$\frac{R_j^{n+1} - R_j^n}{\Delta t} = u_j^{n+1}. \quad (\text{A1})$$

The conservation of momentum equation is:

$$\frac{u_j^{n+1} - u_j^n}{\Delta t} = -\frac{1}{\rho_o} \frac{(\delta p)_j^n}{\Delta r} \left(\frac{R_j^n}{r_j} \right)^2. \quad (\text{A2})$$

The conservation of mass equation is:

$$\rho_{j+1/2}^{n+1} = \rho_o \frac{(r_{j+1})^3 - (r_j)^3}{(R_{j+1}^{n+1})^3 - (R_j^{n+1})^3}. \quad (\text{A3})$$

The First Law of Thermodynamics is:

$$U_{j+1/2}^{n+1} = U_{j+1/2}^n - \left(\frac{p_{j+1/2}^{n+1} + p_{j+1/2}^n}{2} \right) \times \left(\frac{1}{\rho_{j+1/2}^{n+1}} - \frac{1}{\rho_{j+1/2}^n} \right). \quad (\text{A4})$$

Where U = internal energy / mass. The acceleration of the innermost shell is determined by treating its volume as filled with a gas of uniform pressure so that the shell's equation of motion is:

$$m_{inner} \frac{\partial v}{\partial t} = 4\pi(p_{inner} - p_{outer}) \Rightarrow u_0^{n+1} = u_0^n + 4\pi\Delta t(p_{inner} - p_{outer}). \quad (\text{A5})$$

The pressure within the inner sphere varies adiabatically as the shell moves, *i.e.*,

$$p_{inner}(t) = p_o \left(\frac{V_o}{V(t)} \right)^\gamma. \quad (\text{A6})$$

These equations are completed by some equation of state,

$$p_{j+1/2}^{n+1} = f(U_{j+1/2}^{n+1}, \rho_{j+1/2}^{n+1}). \quad (\text{A7})$$

If this equation of state can be algebraically solved, the full set of equations is explicit; if it cannot be solved, then an implicit step and numerical root-finding procedure is required to advance the grid. The advancement of the grid proceeds as follows. 1) Using the conservation of momentum, the new gas velocities are set throughout the system. 2) Boundary conditions are applied. 3) The shell position, R , is advanced according to the new gas velocities. 4) R is then used to set the density throughout the system. 5) Two possibilities: if the equation of state is explicitly soluble, then the internal energy of the gas is determined. If not, then the pressure and energy equations must be stated in terms of the temperature and then solved, together with the First Law, numerically – three equations for three variables, p , U , and T . The above prescription must be modified slightly to accommodate shock fitting. To this end, we introduce an artificial viscous pressure, q , given by the differenced form,

$$q_{j+1/2}^n = \begin{cases} \frac{2a^2[(\delta u)_{j+1/2}^n]^2}{1/\rho_{j+1/2}^n + 1/\rho_{j+1/2}^{n-1}} & \text{if } (\delta u)_{j+1/2}^n < 0 \\ 0 & \text{if } (\delta u)_{j+1/2}^n \geq 0 \end{cases} \quad (\text{A8})$$

Note the parameter, a , which controls how widely the viscous pressure spreads the shock. Optimal values are $1.5 < a < 2.0$, which spread the shock over 3-10 zones. This artificial viscous pressure is added to the regular gas pressure in the above equations as follows: In the conservation of momentum equation,

$$(\delta p)_j^n \rightarrow (\delta p)_j^n + (\delta q)_j^n \quad (\text{A9})$$

and in the energy conservation equation,

$$\frac{p_{j+1/2}^{n+1} + p_{j+1/2}^n}{2} \rightarrow \frac{p_{j+1/2}^{n+1} + p_{j+1/2}^n}{2} + q_{j+1/2}^{n+1}. \quad (\text{A10})$$

When advancing the grid with artificial viscous pressure, the artificial viscosity term, q , is advanced before the energy equation, step 5 in the previous description.

APPENDIX B: SETTING UP MASS SHELLS IN A POLYTROPE

In the initial configuration whose mass and radius are M_* and R_* , define a mass coordinate $\hat{m} = M/M_*$ so that the shell is at radius $\hat{r}(\hat{m}) = R(M)/R_*$.

Let the pressure and density be $P(M) = \hat{P}(\hat{m})(GM_*^2/R_*^4)$ and $\rho(M) = \hat{\rho}(\hat{m})M_*/R_*^3$, respectively. At the centre of the stellar model, we can find $\hat{P}(0) = f_P(n)$ and $\hat{\rho}(0) = f_\rho(n)$, where n is the polytropic index. At any other point in the stellar model, we have $\rho(M) = \rho(0)\theta^n$ and $P(M) = P(0)\theta^{n+1}$. Thus, we have

$$\hat{P}(\hat{m}) = f_P(n)[\theta(\hat{m})]^{n+1} \quad \hat{\rho}(\hat{m}) = f_\rho(n)[\theta(\hat{m})]^n. \quad (\text{B1})$$

Usually, we specify the Lane-Emden function as a function of a dimensionless radius. Getting $\hat{r}(\hat{m})$ then requires a little bit of work. The method is this: the mass inside a physical radius R is

$$M(R) = 4\pi \int_0^R dr r^2 \rho(r) = 4\pi r_{\text{scale}}^3 \int_0^x dx x^2 [\theta(x)]^n, \quad (\text{B2})$$

where r_{scale} is the radius scale. Divide by the total mass to get the conversion equation

$$\hat{m} = \frac{\int_0^x dx x^2 [\theta(x)]^n}{\int_0^{x_0(n)} dx x^2 [\theta(x)]^n} = \frac{\int_0^{x_0(n)\hat{r}(\hat{m})} dx x^2 [\theta(x)]^n}{\int_0^{x_0(n)} dx x^2 [\theta(x)]^n}, \quad (\text{B3})$$

where $\theta(x_0(n)) = 0$ and we have used the fact that the scaled Lane-Emden radius variable $x = x_0(n)\hat{r}(\hat{m})$. This equation can be inverted numerically to get $\hat{r}(\hat{m})$, and we can use the result to evaluate the pressure and density:

$$\begin{aligned} \hat{P}(\hat{m}) &= f_P(n)[\theta(x_0(n)\hat{r}(\hat{m}))]^{n+1} \\ \hat{\rho}(\hat{m}) &= f_\rho(n)[\theta(x_0(n)\hat{r}(\hat{m}))]^n. \end{aligned}$$

We are interested in polytropic models where the pressure is supplied by a mixture of radiation and a nonrelativistic gas. The total pressure in physical units is then

$$P = \frac{\rho k T}{\mu} + \frac{1}{3} a T^4 = P_{\text{gas}} + P_{\text{radiation}}, \quad (\text{B4})$$

where μ is the mass per nonrelativistic particle in the stellar model. We define s

$$s = \frac{P_{\text{radiation}}}{P_{\text{gas}}} = \frac{a T^3 \mu}{3 \rho k}, \quad (\text{B5})$$

which varies throughout the stellar model. At any point in the stellar model, we can use this to eliminate temperature in favor of s :

$$\begin{aligned} T &= \left(\frac{3 \rho s k}{a \mu} \right)^{1/3} \Rightarrow \\ P &= \frac{\rho k T (1+s)}{\mu} = \left(\frac{\rho k}{\mu} \right)^{4/3} \left(\frac{3s}{a} \right)^{1/3} (1+s). \end{aligned}$$

From this it follows that

$$\begin{aligned} \frac{P}{P(0)} &= \left(\frac{\rho}{\rho(0)} \right)^{1+1/n} = [\theta((x_0(n)\hat{r}(\hat{m})))^{n+1} \\ &= \left(\frac{\rho}{\rho(0)} \right)^{4/3} \left(\frac{s}{s(0)} \right)^{1/3} \left(\frac{1+s}{1+s(0)} \right) \\ &= [\theta((x_0(n)\hat{r}(\hat{m})))^{4n/3} \left(\frac{s}{s(0)} \right)^{1/3} \left(\frac{1+s}{1+s(0)} \right), \end{aligned}$$

We can use this to solve for $s(\hat{m})$ via

$$[s(\hat{m})]^{1/3} [1+s(\hat{m})] = [s(0)]^{1/3} [1+s(0)] [\theta(x_0(n)\hat{r}(\hat{m}))]^{1-n/3}.$$

The thermal or internal energy density inside the stellar model is, in physical units,

$$\begin{aligned} \rho U &= \frac{3 \rho k T}{2 \mu} + a T^4 = \frac{3 \rho k T}{2 \mu} (1+2s) \\ &= \frac{3}{2} \left(\frac{\rho k}{\mu} \right)^{4/3} \left(\frac{3s}{a} \right)^{1/3} (1+2s); \end{aligned} \quad (\text{B6})$$

compare this with the pressure

$$P = \left(\frac{\rho k}{\mu} \right)^{4/3} \left(\frac{3s}{a} \right)^{1/3} (1+s). \quad (\text{B7})$$

Define $\gamma(\hat{m})$ by $P = (\gamma(\hat{m}) - 1)\rho U$, to find that

$$\frac{\rho U}{P} = (\gamma(\hat{m}) - 1)^{-1} = \frac{3}{2} \left[\frac{1+2s(\hat{m})}{1+s(\hat{m})} \right]; \quad (\text{B8})$$

let $U = (GM_*/R_*)\hat{U}$ to find that

$$\hat{U}(\hat{m}) = \frac{3f_P(n)}{2f_\rho(n)} \theta(x_0(n)\hat{r}(\hat{m})) \left[\frac{1+2s(\hat{m})}{1+s(\hat{m})} \right]. \quad (\text{B9})$$

This completes the setup of the initial conditions of the polytrope.

We will also need to have the total energy of the stellar model because we want to choose the blast energy as a fraction of the binding energy. The gravitational energy of a polytrope of index n is

$$E_{\text{grav}} = -\frac{3GM_*^2}{(5-n)R_*}. \quad (\text{B10})$$

The internal energy of the stellar model is

$$\begin{aligned} E_{\text{int}} &= 4\pi \int_0^{R_*} dr r^2 \rho(r) U(r) = \int_0^{M_*} dM U(M) \\ &= \frac{3f_P(n)GM_*^2}{2f_\rho(n)R_*} \int_0^1 d\hat{m} \theta(x_0(n)\hat{r}(\hat{m})) \left[\frac{1+2s(\hat{m})}{1+s(\hat{m})} \right]. \end{aligned}$$

This is enough to get the total energy, but we can be a slight bit more elegant by using the virial theorem,

$$\begin{aligned} -E_{\text{grav}} &= 3 \int dM \frac{P}{\rho} \\ &= \frac{3f_P(n)GM_*^2}{f_\rho(n)R_*} \int_0^1 d\hat{m} \theta(x_0(n)\hat{r}(\hat{m})), \end{aligned} \quad (\text{B11})$$

from which we find that

$$\begin{aligned} E_{\text{tot}} &= -\frac{3GM_*^2}{2(5-n)R_*} \times \\ &\quad \left[\frac{\int_0^1 d\hat{m} \theta(x_0(n)\hat{r}(\hat{m})) [1+s(\hat{m})]^{-1}}{\int_0^1 d\hat{m} \theta(x_0(n)\hat{r}(\hat{m}))} \right]. \end{aligned} \quad (\text{B12})$$

If we define $E_{\text{tot}} = -\hat{E}_{\text{tot}} [3GM_*^2/2(5-n)R_*]$ we see that

$$\hat{E}_{\text{tot}} = \frac{\int_0^1 d\hat{m} \theta(x_0(n)\hat{r}(\hat{m})) [1+s(\hat{m})]^{-1}}{\int_0^1 d\hat{m} \theta(x_0(n)\hat{r}(\hat{m}))} \quad (\text{B13})$$

$$= \frac{\int_0^1 d\hat{m} \frac{\hat{P}(\hat{m})}{\hat{\rho}(\hat{m})} [1+s(\hat{m})]^{-1}}{\int_0^1 d\hat{m} \frac{\hat{P}(\hat{m})}{\hat{\rho}(\hat{m})}}. \quad (\text{B14})$$

APPENDIX C: DYNAMICAL EQUATIONS

The equation of motion for a mass shell is

$$\frac{\partial^2 R(M, t)}{\partial t^2} = -4\pi R^2(M, t) \frac{\partial P(M, t)}{\partial M} - \frac{GM}{R^2(M, t)} + a_{\text{visc}}(M, t), \quad (\text{C1})$$

where $a_{\text{visc}}(M, t)$ is the viscous acceleration (which we include using a prescribed artificial viscosity). Introducing our nondimensional radius, pressure and mass implies

$$\begin{aligned} R_* \frac{\partial^2 \hat{r}(\hat{m}, t)}{\partial t^2} &= \frac{GM_*}{R_*^2} \left[-4\pi \hat{r}^2(\hat{m}, t) \frac{\partial \hat{P}(\hat{m}, t)}{\partial \hat{m}} - \right. \\ &\quad \left. \frac{\hat{m}}{\hat{r}^2(\hat{m}, t)} \right] + a_{\text{visc}}(\hat{m}, t); \end{aligned} \quad (\text{C2})$$

Define a dimensionless time by $t = (R_*^3/GM_*)^{1/2} \tau$; then

$$\frac{\partial^2 \hat{r}(\hat{m}, \tau)}{\partial \tau^2} = -4\pi \hat{r}^2(\hat{m}, \tau) \frac{\partial \hat{P}(\hat{m}, \tau)}{\partial \hat{m}}$$

$$-\frac{\hat{m}}{\hat{r}^2(\hat{m}, \tau)} + \hat{a}_{\text{visc}}(\hat{m}, \tau), \quad (\text{C3})$$

where the viscous acceleration is defined by $a_{\text{visc}}(M, t) = \hat{a}_{\text{visc}}(\hat{m}, \tau)(GM_\star/R_\star^2)$. Since we shall actually want equations that are first order in time, we note that the radial velocity is

$$\begin{aligned} \frac{\partial R(M, t)}{\partial t} &= \left(\frac{GM_\star}{R_\star}\right)^{1/2} \frac{\partial \hat{r}(\hat{m}, \tau)}{\partial \tau} \\ &= \left(\frac{GM_\star}{R_\star}\right)^{1/2} \hat{v}(\hat{m}, \tau), \end{aligned} \quad (\text{C4})$$

and therefore

$$\begin{aligned} \frac{\partial \hat{r}(\hat{m}, \tau)}{\partial \tau} &= \hat{v}(\hat{m}, \tau) \\ \frac{\partial \hat{v}(\hat{m}, \tau)}{\partial \tau} &= -4\pi\hat{r}^2(\hat{m}, \tau) \frac{\partial \hat{P}(\hat{m}, \tau)}{\partial \hat{m}} \\ &\quad - \frac{\hat{m}}{\hat{r}^2(\hat{m}, \tau)} + \hat{a}_{\text{visc}}(\hat{m}, \tau). \end{aligned} \quad (\text{C5})$$

From the first law of thermodynamics, we get that

$$\frac{\partial U(M, t)}{\partial t} = q_{\text{visc}}(M, t) - P(M, t) \frac{\partial}{\partial t} \left[\frac{1}{\rho(M, t)} \right], \quad (\text{C6})$$

where $q_{\text{visc}}(M, t)$ is the viscous heating, which we take to be

$$q_{\text{visc}}(M, t) = \begin{cases} -a^2 \rho(M, t) \left(\frac{\partial v}{\partial R}\right)^2 \frac{\partial}{\partial t} \left[\frac{1}{\rho(M, t)} \right] & \text{if } \left(\frac{\partial v}{\partial R}\right) < 0 \\ 0 & \text{if } \left(\frac{\partial v}{\partial R}\right) \geq 0 \end{cases}$$

where a is a constant with units of length. Introducing the same nondimensional variables as in the polytrope setup we find that

$$\begin{aligned} \frac{\partial \hat{U}(\hat{m}, \tau)}{\partial \tau} &= - \left(a^2 \hat{\rho}(\hat{m}, \tau) \left(\frac{\partial \hat{v}}{\partial \hat{r}}\right)^2 + \hat{P}(\hat{m}, \tau) \right) \times \\ &\quad \frac{\partial}{\partial \tau} \left[\frac{1}{\hat{\rho}(\hat{m}, \tau)} \right], \end{aligned} \quad (\text{C7})$$

where the viscous heating is defined by $q_{\text{visc}} = \hat{q}_{\text{visc}}[(GM_\star)^{3/2}/R_\star^{5/2}]$. We can replace the pressure by

$$P = \frac{2\rho U}{3} \left(\frac{1+s}{1+2s} \right) \Rightarrow \hat{P} = \frac{2\hat{\rho}\hat{U}}{3} \left(\frac{1+s}{1+2s} \right) \quad (\text{C8})$$

to rewrite the first law in the form

$$\begin{aligned} \frac{\partial \hat{U}(\hat{m}, \tau)}{\partial \tau} &= \left(\frac{a^2}{\hat{\rho}(\hat{m}, \tau)} \left(\frac{\partial \hat{v}}{\partial \hat{r}}\right)^2 + \right. \\ &\quad \left. \frac{2\hat{U}(\hat{m}, \tau)[1+s(\hat{m}, \tau)]}{3\hat{\rho}(\hat{m}, \tau)[1+2s(\hat{m}, \tau)]} \right) \frac{\partial \hat{\rho}(\hat{m}, \tau)}{\partial \tau}. \end{aligned} \quad (\text{C9})$$

We can close the loop using $U \propto \rho^{1/3} s^{1/3} (1+2s)$ to get

$$\frac{\hat{U}(\hat{m}, \tau)}{\hat{U}(\hat{m}, 0)} = \left(\frac{\hat{\rho}(\hat{m}, \tau)s(\hat{m}, \tau)}{\hat{\rho}(\hat{m}, 0)s(\hat{m}, 0)} \right)^{1/3} \left[\frac{1+2s(\hat{m}, \tau)}{1+2s(\hat{m}, 0)} \right]. \quad (\text{C10})$$

We could use this to find an equation for $s(\hat{m}, \tau)$ explicitly; then

$$\begin{aligned} \frac{\partial}{\partial \tau} \left[\frac{s(\hat{m}, \tau)e^{8s(\hat{m}, \tau)}}{\hat{\rho}(\hat{m}, \tau)} \right] &= \left\{ \frac{3q_{\text{visc}}(\hat{m}, \tau)[1+2s(\hat{m}, \tau)]}{U(\hat{m}, \tau)} \right\} \times \\ &\quad \frac{s(\hat{m}, \tau)e^{8s(\hat{m}, \tau)}}{\hat{\rho}(\hat{m}, \tau)}, \end{aligned} \quad (\text{C11})$$

with $\hat{U}(\hat{m}, \tau)$ evaluated using Eq. (C10). Finally, the equation of mass conservation can be written as

$$\begin{aligned} \frac{1}{\rho(M, t)} &= 4\pi r^2(M, t) \frac{\partial r(M, t)}{\partial M} \Rightarrow \\ \frac{1}{\hat{\rho}(\hat{m}, \tau)} &= 4\pi \hat{r}^2(\hat{m}, \tau) \frac{\partial \hat{r}(\hat{m}, \tau)}{\partial \hat{m}}. \end{aligned} \quad (\text{C12})$$

If we wish, we can define a new variable $\hat{V}(\hat{m}, \tau) = 1/\hat{\rho}(\hat{m}, \tau)$, and rewrite the last few equations as

$$\begin{aligned} \hat{V}(\hat{m}, \tau) &= 4\pi \hat{r}^2(\hat{m}, \tau) \frac{\partial \hat{r}(\hat{m}, \tau)}{\partial \hat{m}} \\ \frac{\hat{U}(\hat{m}, \tau)}{\hat{U}(\hat{m}, 0)} &= \left[\frac{\hat{V}(\hat{m}, 0)s(\hat{m}, \tau)}{\hat{V}(\hat{m}, \tau)s(\hat{m}, 0)} \right]^{1/3} \left[\frac{1+2s(\hat{m}, \tau)}{1+2s(\hat{m}, 0)} \right] \\ \frac{\partial \hat{U}(\hat{m}, \tau)}{\partial \tau} &= - \left(\frac{a^2}{V(\hat{m}, \tau)} \left(\frac{\partial \hat{v}}{\partial \hat{r}}\right)^2 \right. \\ &\quad \left. + \frac{2\hat{U}(\hat{m}, \tau)[1+s(\hat{m}, \tau)]}{3\hat{V}(\hat{m}, \tau)[1+2s(\hat{m}, \tau)]} \right) \frac{\partial \hat{V}(\hat{m}, \tau)}{\partial \tau} \end{aligned} \quad (\text{C13})$$

Eqs. (C5), and either Eqs. (C9), (C10) and (C12) or Eqs. (C13), with the initial conditions set up in the previous sections, can now be cast into finite difference form, with a suitable specification of the artificial viscous force and heating.

For all calculations done after the code was tested, we also included a Newtonian Gravitation force per unit mass via

$$F_{\text{grav}} = -\frac{GM(R)}{R^2}, \quad (\text{C14})$$

or in difference form,

$$F_j^n = -\frac{G\rho_o \frac{4\pi}{3} (r_j^n)^3}{(R_j^n)^2}. \quad (\text{C15})$$

This force was added to the conservation of momentum equation, the equation used to set gas velocities. Finally, the code self-checks by calculating total energy and momentum to ensure that these are conserved. For energy, the sum of the local energy in each zone is calculated first *via*

$$E_{\text{kinetic}} + E_{\text{therm}} = \sum_{i \in \text{zones}} \left(\frac{1}{2} u_i^2 + U_i \right) \Delta M_i. \quad (\text{C16})$$

The gravitational potential energy is then calculated via

$$E_{\text{grav}} = - \sum_{i \in \text{zones}} \frac{GM_{\text{enclosed}}}{R_i} \Delta M_i. \quad (\text{C17})$$

and the two energies are added and recorded as the current total energy in the system. Conservation of momentum is also checked though a simple summation:

$$P_{\text{tot}} = \sum_{i \in \text{zones}} u_{\text{zone}} \Delta M_i. \quad (\text{C18})$$

Finally, the algebraic equation used to determine the total local energy per unit mass of each zone – the quantity used to determine if a zone was bound or unbound – was

$$\begin{aligned} \frac{E_{\text{zone}=j}^{\text{tot}}}{\Delta M_j} &= \frac{E_j^{\text{therm}} + E_j^{\text{kinetic}} + E_j^{\text{potential}}}{\Delta M_j} \\ &= \frac{1}{2} u_j^2 + U_j - \frac{1}{2} \sum_{i=1}^{i \leq j} F_i^{\text{grav}} \Delta R_i, \end{aligned} \quad (\text{C19})$$

where $\Delta R_i = R_i - R_{i-1}$.

APPENDIX D: SEDOV SOLUTION

For the analytic solution to the Sedov problem, we rederived the solution given in Landau and Lifshitz's *Fluid Mechanics*, thereby finding the correction to an error (in an exponent) that is mentioned in Shu's *Gas Dynamics*. Rather than re-reporting the entire result, we simply note that the correction comes in the exponents of the equation for ρ :

$$\rho \propto \left(\left(\frac{\gamma + 1}{\gamma - 1} \right) \left(1 - \frac{5t}{2r} v \right) \right)^{\nu_5} \quad (\text{D1})$$

where

$$\nu_5 = -\frac{2}{2 - \gamma}.$$